

1 An analytical and numerical investigation of acoustic
2 attenuation by a sonic crystal array

3 H. Chung^a, F. Montiel^b, M. Karimi^c, N. Kessissoglou^c

4 ^a*School of Computer and Mathematical Sciences, Auckland University of Technology, Auckland,*
5 *New Zealand*

6 ^b*Department of Mathematics and Statistics, University of Otago, Dunedin, New Zealand*

7 ^c*School of Mechanical and Manufacturing Engineering, UNSW Australia, Sydney, Australia*

8 **Abstract**

Sonic crystals are scatterers arranged periodically in a homogeneous fluid medium, for which sound does not transmit through the crystal in certain frequency bands known as stop bands. Acoustic wave transmission through a two-dimensional sonic crystal composed of a finite array of scatterers is investigated. Two types of scatterers are considered: sound-hard cylinders and C-shaped locally resonant scatterers. An analytical method is devised to solve the corresponding multiple scattering problems. The method combines an integral equation technique for the single scatterer with an enhanced multipole method using domain decomposition into slabs. A numerical approach using commercial software is also considered for validation and is based on the finite element method. Simulations of sound transmission through an array of 5 by 51 scatterers show remarkably good agreement with the corresponding infinite system. For an array comprising locally resonant scatterers, an approximate band gap around the resonator natural frequency is observed in addition to the band gap due to the overall periodicity of the sonic crystal array.

9 *Keywords:* sonic crystal, multiple scattering, analytical method, finite element

11 **1. Introduction**

12 Sonic crystals are periodic arrangements of acoustic scatterers embedded in a fluid
13 medium [1]. An interesting property of infinite crystals is the occurrence of ranges
14 of frequencies in which propagation of sound is prohibited, as a result of destructive
15 interferences. Such frequency ranges are referred to as Bragg band gaps and are a
16 function of the spacing between adjacent scatterers only. Periodic arrays of scatterers
17 have been studied for a range of applications, e.g. as sonic crystal barriers to reduce
18 traffic noise pollution [2–4], as floating ice floes to observe wave attenuation in the
19 marginal ice zone [5–7], as bubble phononic crystals for acoustic tiling [8, 9], and as
20 photonic crystals [10].

21 A plethora of work related to periodic arrays of scatterers can be found in literature.
22 As such the following review is by no means exhaustive. Linton and Thompson [11]
23 investigated the effect of frequency, incident angle and array spacing on scattering of
24 plane acoustic waves by an infinite periodic array of circles. Bennetts [6] proposed
25 a method to analytically predict wave scattering by a multiple-row array of periodic
26 scatterers in which the rows were permitted to have different periodicities.

27 Well-known prediction models for wave interactions with sonic crystals include mul-
28 tiple scattering theory (MST) [12–15], plane wave expansion (PWE) [16] and the finite
29 difference time domain method (FDTD) [17]. An early review on sonic crystals was
30 presented by Miyashita [17]. More recently, Gupta [18] reviewed applications of sonic
31 crystals and numerical methods to study their acoustic performance. Gupta et al. [19]
32 designed a radial sonic crystal based on the Webster horn equation, which consists of

33 periodic structures in polar coordinates.

34 The concept of a sonic crystal barrier, first introduced by Martinez-Sala et al. [2], has
35 received much interest, for example, see [3, 12, 13, 15, 20–24]. The performance of a two-
36 dimensional arrangement of rigid hollow cylinders in air was investigated by Sanchez-
37 Perez et al. [3]. Vasseur et al. [21] theoretically and experimentally examined sound
38 attenuation by a square array of parallel copper cylinders. Their results revealed that
39 rigid hollow and solid cylinders produce similar sound transmission. Jean and Defrance
40 [20] used a 2D boundary integral formulation to examine the acoustic performance of
41 a sonic crystal noise barrier comprising rows of cylinders of infinite extent. Romero-
42 García et al. [24] studied the effect of the interaction between a sonic crystal barrier
43 and the ground on the barrier acoustic performance. Full-space and half-space sonic
44 crystal barrier problems comprising arrays of rigid and porous cylinders were recently
45 studied using the FDTD approach coupled with the immersed boundary method [25].

46 Since the seminal paper by Liu et al. [26], the acoustic performance of a sonic crystal
47 comprised of locally resonant scatterers has also attracted recent significant attention
48 [4, 15, 20, 26–33]. Koussa et al. [4] combined a sonic crystal aligned parallel to the
49 ground with a rigid straight noise barrier. To further extend the barrier insertion loss,
50 the scatterers were modelled as either rigid cylinders or resonant cavities, where the
51 cavities were either reactive or lined with an absorbent material. Chalmers et al. [30]
52 showed that the use of locally resonant C-shaped scatterers in a periodic arrangement
53 results in the generation of locally resonant band gaps around the Helmholtz resonator
54 frequency in addition to the Bragg band gap due to the periodicity of the sonic crystal
55 array. However, the sub-Bragg band gap generated by the locally resonant scatterers
56 is generally very narrow in bandwidth [31]. Elford et al. [32] showed that by designing

57 the locally resonant scatterers in a Russian doll or Matryoshka configuration, a broader
58 band gap can be achieved.

59 In this work, we investigate the acoustic performance of a finite sonic crystal in
60 approximating the known band gap structure of the corresponding infinite array. We
61 seek to reproduce both Bragg and sub-Bragg band gaps by considering both sound-hard
62 and C-shaped locally resonant scatterers. An efficient analytical technique is proposed
63 to calculate the transmitted field by the finite array. An integral equation/Galerkin
64 method is used to describe the scattering by an individual scatterer, while we apply the
65 domain decomposition technique of Montiel et al. [34] to resolve multiple scattering
66 in the array. The results are compared with predictions made using the commercial
67 finite element package COMSOL Multiphysics (v5.1). The quantity of interest is the
68 transmission loss, which is defined as the reduction of sound pressure level behind the
69 array due to the presence of the array. We examine how the transmission loss is affected
70 by the properties of the C-shaped resonator.

71 **2. Preliminaries**

72 Consider the scattering of sound waves in two dimensions by a sonic crystal array
73 that consists of a finite number of scatterers arranged in a square lattice with regular
74 spacing d in both horizontal dimensions. The array is composed of S rows, each con-
75 taining J_c scatterers. We use the Cartesian coordinates (x, y) to locate points in the
76 infinite plane. The x and y axes are oriented in the direction of the lattice vectors, as
77 shown in Figure 1a.

78 The host medium is air and is assumed to be homogeneous. We further consider
79 the air medium to be lossless, so wave energy is redistributed spatially as a result of

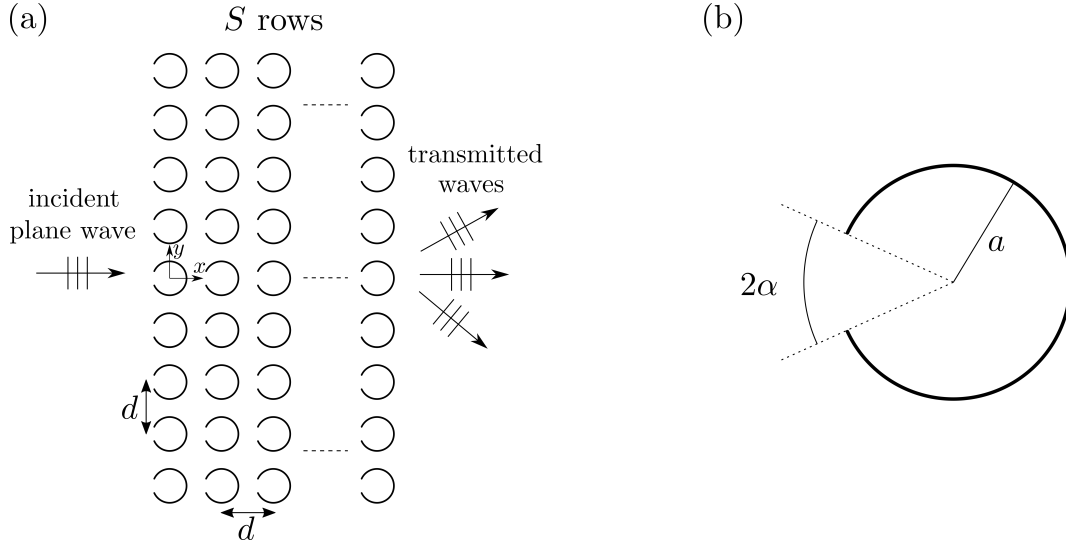


Figure 1: (a) A finite sonic crystal array composed of S rows of C-shaped scatterers with lattice constant d in both horizontal directions. (b) A single C-shaped scatterer (resonator) with radius a and opening angle 2α .

80 scattering but is preserved.

81 All the scatterers are identical C-shaped cylindrical resonators with radius a and
 82 opening angle 2α (see Figure 1b). The origin of the Cartesian coordinate system
 83 coincides with the centre of the middle scatterer in the first row, assuming an odd
 84 number J_c scatterer in each row. In row s , the centre of scatterer j has coordinates
 85 $(x_s, y_j) = ((s - 1)d, (j - 1 - (J_c - 1)/2)d)$. The resonator shell is assumed to be rigid
 86 and to have a small thickness compared to the acoustic wavelength. Under this condi-
 87 tion, the thickness of the shell can be neglected (this assumption was further validated
 88 numerically using the method described in §4).

89 Assuming time-harmonic conditions with radian frequency ω , the acoustic pressure
 90 is given by $\text{Re}\{p(x, y) \exp(-i\omega t)\}$. The (reduced) complex pressure p satisfies the

91 Helmholtz equation [35]

$$\nabla^2 p + k^2 p = 0 \tag{1}$$

92 where we have introduced the acoustic wavenumber $k = \omega/c$, everywhere in the host
93 medium.

94 For each C-shaped scatterer j in a given row, we introduce the local polar coordinates
95 (r_j, θ_j) with origin at the centre of cylinder j . Considering sound-hard boundaries, the
96 pressure satisfies

$$\frac{\partial p}{\partial r_j} = 0, \quad r_j = a, \quad \theta_j \in \Gamma_c, \tag{2}$$

97 for each cylinder $j = 1, \dots, J_c$. We have introduced $\Gamma_c = \{\theta_j, -\pi + \alpha < \theta_j < \pi - \alpha\}$.
98 Note that this condition applies for both the interior ($r_j < a$) and exterior ($r_j > a$)
99 fields to the scatterer.

100 An ambient plane wave field with unit amplitude and normally incident on the
101 array (i.e. travelling along the direction of the positive x -axis) is prescribed to force a
102 non-trivial solution. The corresponding pressure field is then given by

$$p_{\text{am}}(x, y) = e^{ikx}. \tag{3}$$

103 We seek to describe the scattered field $p - p_{\text{am}}$ arising from multiple scattering by the
104 array. Two methods are discussed in what follows to solve this boundary value problem.

105 **3. Analytical method**

106 The first solution method follows closely the domain decomposition technique pro-
107 posed by Montiel et al. [34] for an arbitrary finite array of sound-hard scatterers. We

108 first cluster the array into S slabs defined by $(s-3/2)d < x < (s-1/2)d$ for $s = 1, \dots, S$.

109 Therefore, each slab s contains the J_c scatterers in the s th row of the sonic crystal.

110 We seek the far-field transmitted acoustic pressure by the array as a superposition
111 of plane waves with amplitude continuously depending on the travelling angle χ with
112 respect to the x axis, that is,

$$p = p_T(x, y) \approx \int_{-\pi/2}^{\pi/2} A_T(\chi) e^{ik(x \cos \chi + y \sin \chi)} d\chi, \quad x \gg Sd, \quad (4)$$

113 where $A_T(\chi)$ is the unknown amplitude of the transmitted field. Note that an analogous
114 expression exists for the reflected field, but in §5, we will only discuss the properties of
115 the transmitted field, so we omit the description of the reflected field in the solution
116 method.

117 3.1. Scattering by a single scatterer

118 We first describe the scattering by a single C-shaped scatterer j in a row of the ar-
119 ray. An integral equation/Galerkin method is devised to find a relationship between an
120 arbitrary incoming wave field and the corresponding outgoing wave field. The method
121 resembles that proposed by [36] for elastic Helmholtz resonators. This method is known
122 to exhibit superior convergence properties compared to a standard eigenfunction match-
123 ing technique [37].

124 We decompose the pressure field into an interior field p_{int}^j for $r_j < a$ and an exterior
125 field p_{ext}^j for $r_j > a$, which is further decomposed into incoming and outgoing waves.

126 The partial multipole expansions of the exterior and interior pressure fields are

$$p_{\text{ext}}^j(r_j, \theta_j) = p_{\text{in}}^j + p_{\text{sc}}^j \approx \sum_{n=-N}^N (a_n^j J_n(kr_j) + c_n^j H_n(kr_j)) e^{in\theta_j}, \quad r_j > a \quad (5)$$

127 and

$$p_{\text{int}}^j(r_j, \theta_j) \approx \sum_{n=-N}^N d_n^j J_n(kr_j) e^{in\theta_j}, \quad r_j < a, \quad (6)$$

128 respectively. Here J_n and H_n are the Bessel and Hankel functions of the first kind of
129 order n , respectively.

130 The boundary condition given by Eq. (2) applies to both the interior and exterior
131 fields

$$\frac{\partial p_{\text{ext}}^j}{\partial r_j} = \frac{\partial p_{\text{int}}^j}{\partial r_j} = 0, \quad r_j = a, \theta_j \in \Gamma_c. \quad (7)$$

132 We further have continuity of pressure and normal velocity at the opening of the C-
133 shaped scatterer, i.e.

$$p_{\text{ext}}^j(r_j, \theta_j) = p_{\text{int}}^j(r_j, \theta_j) \quad \text{and} \quad \frac{\partial p_{\text{int}}^j}{\partial r_j} = \frac{\partial p_{\text{ext}}^j}{\partial r_j}, \quad r_j = a, \theta_j \in \Gamma_g, \quad (8)$$

134 where $\Gamma_g = \{\theta_j, -\alpha < \theta_j - \pi < \alpha\}$.

135 We introduce an auxiliary function $v(\theta_j)$ in the opening of the scatterer which
136 describes the boundary condition there for the interior and exterior fields. These are
137 given by

$$\left. \frac{\partial p_{\text{ext}}^j}{\partial r_j} \right|_{r=a} = v(\theta_j), \quad \theta_j \in \Gamma_g. \quad (9a)$$

138 and

$$\left. \frac{\partial p_{\text{int}}^j}{\partial r_j} \right|_{r=a} = v(\theta_j), \quad \theta_j \in \Gamma_g. \quad (9b)$$

139 Projecting Eqs. (9a) and (9b) with respect to the Fourier basis function $\exp(-in\theta_j)$
 140 yields

$$\int_{\Gamma_g} v(\theta_j) e^{-in\theta_j} d\theta_j = \int_0^{2\pi} \left. \frac{\partial p_{\text{ext}}}{\partial r_j} \right|_{r=a} e^{-in\theta_j} d\theta_j = 2\pi k (J'_n(ka) a_n^j + H'_n(ka) c_n^j) \quad (10)$$

141 and

$$\int_{\Gamma_g} v(\theta_j) e^{-in\theta_j} d\theta_j = \int_0^{2\pi} \left. \frac{\partial p_{\text{int}}}{\partial r_j} \right|_{r_j=a} e^{-in\theta_j} d\theta_j = 2\pi k J'_n(ka) d_n^j, \quad (11)$$

142 respectively, where we have used Eq.(7) to extend the integration domain of the interior
 143 and exterior normal derivatives and the orthogonality of the Fourier basis functions.
 144 We can then express the exterior and interior scattered wave coefficients in terms of the
 145 auxiliary function as

$$c_n^j = Z_n a_n^j + \frac{1}{2\pi k H'_n(ka)} \int_{\Gamma_g} v(\theta_j) e^{-in\theta_j} d\theta_j, \quad (12)$$

146 where $Z_n = -J'_n(ka)/H'_n(ka)$, and

$$d_n^j = \frac{1}{2\pi k J'_n(ka)} \int_{\Gamma_g} v(\theta_j) e^{-in\theta_j} d\theta_j. \quad (13)$$

147 Continuity of the pressure across the opening given by Eq. (8) yields

$$\sum_{n=-N}^N \{a_n^j J_n(ka) + c_n^j H_n(ka)\} e^{in\theta_j} = \sum_{n=-N}^N d_n^j J_n(ka) e^{in\theta_j}. \quad (14)$$

Substituting c_n^j and d_n^j in Eq. (14) using Eqs. (12) and (13), we obtain

$$\begin{aligned} \sum_{n=-N}^N a_n^j J_n(ka) e^{in\theta_j} + \sum_{n=-N}^N \left(Z_n a_n^j + \frac{1}{2\pi k H_n'(ka)} \int_{\tau \in \Gamma_g} v(\tau) e^{-in\tau} d\tau \right) H_n(ka) e^{in\theta_j} \\ = \sum_{n=-N}^N \left(\frac{1}{2\pi k J_n'(ka)} \int_{\tau \in \Gamma_g} v(\tau) e^{-in\tau} d\tau \right) J_n(ka) e^{in\theta_j} \end{aligned} \quad (15)$$

148 valid for $\theta_j \in \Gamma_g$. Rearranging Eq. (15), we obtain the following integral equation

$$\int_{\Gamma_g} K(\theta_j : \tau) v(\tau) d\tau = f^{(j)}(\theta_j) \quad (16)$$

149 to be solved for the auxiliary function $v(\tau)$. The kernel $K(\theta_j : \tau)$ and forcing term
150 $f(\theta_j)$ are given by

$$K(\theta_j : \tau) = \sum_{n=-N}^N \mathcal{K}_n e^{in(\theta_j - \tau)} \quad \text{and} \quad f^{(j)}(\theta_j) = 2\pi k \sum_{n=-N}^N a_n^j \mathcal{K}_n J_n'(ka) e^{in\theta_j}, \quad (17)$$

151 respectively, where

$$\mathcal{K}_n = \frac{J_n(ka)}{J_n'(ka)} - \frac{H_n(ka)}{H_n'(ka)} = \frac{2i}{\pi ka J_n'(ka) H_n'(ka)}.$$

152 A Wronskian identity was used to simplify \mathcal{K}_n .

153 The integral equation is solved numerically using the Galerkin technique. We expand
154 the auxiliary function in its Fourier representation on the domain Γ_g , that is

$$v(\tau) \approx \sum_{m=-M}^M b_m e^{iK_m \tau}, \quad \tau \in \Gamma_g, \quad (18)$$

155 where $K_m = m\pi/\alpha$. Substituting Eq. (18) in Eq. (16) and projecting on $e^{-iK_p\theta_j}$ for
 156 $\theta_j \in \Gamma_g$, the following linear system for $\mathbf{b} = (b_{-M}, \dots, b_M)^\top$ is obtained

$$\mathbf{K}\mathbf{b} = 2\pi k\mathbf{F}^{(j)} \quad (19)$$

157 where the matrix \mathbf{K} and vector $\mathbf{F}^{(j)}$ have dimension $(2M+1) \times (2M+1)$ and $2M+1$,
 158 respectively, and are given by

$$\mathbf{K} = \mathbf{A}\mathcal{K}\mathbf{A}^* \quad \text{and} \quad \mathbf{F}^{(j)} = \mathbf{A}\mathcal{K}\mathbf{D}_J\mathbf{a}^j.$$

159 We have introduced the matrix \mathbf{A} of dimension $(2M+1) \times (2N+1)$ with entries

$$A_{m,n} = \int_{\Gamma_g} e^{-iK_m\theta_j} e^{in\theta_j} d\theta_j = 2\alpha e^{i(n\alpha - m\pi)\frac{\pi}{\alpha}} \text{sinc}(n\alpha/\pi - m)$$

160 where $\text{sinc } x = \sin \pi x / \pi x$, and the diagonal matrices \mathcal{K} and \mathbf{D}_J have dimension $(2N+1) \times (2N+1)$ with entries \mathcal{K}_n and $J'_n(ka)$, respectively. The superscript $*$ was used to
 161 denote the conjugate transpose of a matrix.
 162

163 The accuracy of the solution method depends mainly on the accuracy of the kernel
 164 matrix \mathcal{K} in the expression of \mathbf{K} . To compute the latter matrix, we therefore increase
 165 the size of \mathcal{K} to $\sim 1000 \gg 2N+1$ while expanding the auxiliary function into $M =$
 166 $O(10)$ modes. The size of \mathbf{A} in the expression for \mathbf{K} is modified accordingly. For the
 167 computation of the forcing vector $\mathbf{F}^{(j)}$, the matrix \mathcal{K} remains of size $2N+1$, where
 168 $N = O(1)$. This procedure allows us to obtain 5-digit accuracy for the unknown
 169 amplitudes $\mathbf{c}^j = (c_{-N}^j, \dots, c_N^j)^\top$ and $\mathbf{d}^j = (d_{-N}^j, \dots, d_N^j)^\top$.

170 The mappings between the amplitudes of the exterior and interior scattered fields

171 and those of the incident field are then given by Eqs. (12) and (13), where we substitute
 172 Eqs. (18) and (19) to eliminate the auxiliary function. We obtain

$$\mathbf{c}^j = (\mathbf{Z} + \mathbf{D}_H^{-1} \mathbf{A}^* \mathbf{K}^{-1} \mathbf{A} \mathcal{K} \mathbf{D}_J) \mathbf{a}^j = \mathbf{D} \mathbf{a}^j \quad (20)$$

173 for the exterior mapping, where \mathbf{Z} and \mathbf{D}_H are the diagonal matrices of size $2N + 1$
 174 with entries Z_n and $H'_n(ka)$, respectively, and

$$\mathbf{d}^j = (\mathbf{D}_J^{-1} \mathbf{A}^* \mathbf{K}^{-1} \mathbf{A} \mathcal{K} \mathbf{D}_J) \mathbf{a}^j \quad (21)$$

175 for the interior mapping. We see that the method only requires inversion of the matrix
 176 \mathbf{K} which has size $O(10)$, and is therefore significantly more efficient than the stan-
 177 dard mode matching technique, which typically requires inversion of matrices with size
 178 $O(100)$ or higher for equal or inferior accuracy [37].

179 In the special case of a sound-hard cylinder without an opening, i.e. $\alpha = 0$, the
 180 interior field p_{int}^j is not coupled to the exterior field p_{ext}^j . The mapping for the exterior
 181 fields given in Eq. (20) then becomes

$$\mathbf{c}^j = \mathbf{Z} \mathbf{a}^j. \quad (22)$$

182 In Eq. (20), the matrix $\mathbf{D} = \mathbf{Z} + \mathbf{D}_H^{-1} \mathbf{A}^* \mathbf{K}^{-1} \mathbf{A} \mathcal{K} \mathbf{D}_J$ describing the scattering properties
 183 of the resonator is the superposition of the closed cylinder mapping \mathbf{Z} and a correction
 184 term due to the presence of the gap.

185 *3.2. Scattering by a single row*

186 Wave interaction in a single row of scatterers is resolved using the standard multipole
 187 method described by Martin [13]. We only give a brief summary of the method here and
 188 the reader is referred to excellent aforementioned book or [34]. The total pressure in
 189 the vicinity of scatterer j , for $j = 1, \dots, J_c$, can be expressed as the sum of an incident
 190 field and a scattered field, that is $p^j = p_{\text{in}}^j + p_{\text{sc}}^j$. We enforce coupling between all the
 191 scatterers by writing the incident field as the sum of the incident forcing field p_{inc} and
 192 the scattered field due to all the other scatterers, i.e.

$$p_{\text{in}}^j = p_{\text{inc}} + \sum_{i=1, i \neq j}^{J_c} p_{\text{sc}}^i. \quad (23)$$

193 The incident and scattered fields around scatterer j , p_{in}^j and p_{sc}^j , respectively, are
 194 approximated using the truncated multipole expansions given in Eq. (5). We write
 195 a similar expansion for the incident forcing field p_{inc} in the local polar coordinates of
 196 scatterer j

$$p_{\text{inc}}(r_j, \theta_j) \approx \sum_{n=-N}^N f_n^j J_n(kr_j) e^{in\theta_j}, \quad (24)$$

197 Substituting Eqs. (5) and (24) in (23), applying Graf's addition theorem [38] to express
 198 outgoing polar harmonics from scatterer i as regular polar harmonics into scatterer j ,
 199 and projecting on the incident polar harmonics of order n , we obtain

$$a_n^j = f_n + \sum_{i=1, i \neq j}^{J_c} \sum_{s=-N}^N H_{s-n}(kR_{ij}) e^{i(s-n)\theta_{ij}} c_s^i, \quad (25)$$

200 where $(R_{ij}, \theta_{ij}) = (|j - i|s, \text{sgn}(j - i)\pi/2)$ are the polar coordinates of the centre of the
 201 j^{th} scatterer into the local system associated with the i^{th} cylinder. Rewriting Eq. (25)
 202 in matrix form and using the scattering map for the single scatterer given in Eq. (20),
 203 we obtain

$$\mathbf{c}^j - \sum_{i=1, i \neq j}^{J_c} \sum_{s=-N}^N \mathbf{D} \mathbf{T}_s^{i,j} \mathbf{c}^i = \mathbf{D} \mathbf{f}^j, \quad (26)$$

204 where $\mathbf{f}^j = (f_{-N}^j, \dots, f_N^j)^{\text{T}}$, $\mathbf{T}_s^{i,j} = \text{diag}\{H_{s-n}(kR_{ij})e^{i(s-n)\theta_{ij}}, n = -N, \dots, N\}$ and we
 205 have multiplied across by \mathbf{D} .

206 Equation (26) describes a system of equations that can be solved for \mathbf{c}^j , $j = 1, \dots, J_c$.
 207 The solution can be summarised in a single matrix equation

$$\mathbf{c} = \mathbf{T} \mathbf{f}, \quad (27)$$

208 where \mathbf{c} and \mathbf{f} are column vectors of length $J_c(2N + 1)$ obtained by concatenating \mathbf{c}_j
 209 and \mathbf{f}_j for $j = 1, \dots, J_c$.

210 3.3. Scattering by multiple rows

211 We now consider the full problem described in §2 with S rows. The technique used
 212 to enforce row-row interactions is similar to the S -matrix method commonly used for
 213 solving wave propagation problems through photonic or phononic crystals, in which each
 214 row contains an infinite periodic array of scatterers [see, e.g. 39, 40]. The extension to
 215 finite arbitrary rows was proposed by [34], who also give an extensive literature review
 216 on the use of the S -matrix method in many areas concerned with wave scattering by
 217 infinite regular or partially regular arrays. We only give a summary of the method here
 218 and the reader is referred to [34] for additional details.

We define p_{inc}^s as the incident forcing field on row s and express it as a superposition of plane waves travelling leftward and rightward and with amplitudes that depend continuously on the angle ϕ , with respect to the x -axis. This can be expressed as follows

$$p_{\text{inc}}^s(x, y) = \int_{\Lambda} \left(A_s^+(\phi) e^{i k((x-\xi_{s-1}) \cos \phi + y \sin \phi)} + A_s^-(\phi) e^{i k(-(x-\xi_s) \cos \phi + y \sin \phi)} \right) d\phi, \quad (28)$$

219 where $\xi_s = x_{s+1} - d/2$, for $s = 0, \dots, S$. The functions $A_s^+(\phi)$ and $A_s^-(\phi)$ describe
 220 the amplitude of the plane wave components travelling at angle ϕ with respect to the
 221 x -axis in the positive and negative x direction, respectively. The range of angular
 222 components is a contour Λ that extends in the complex plane. It is composed of the
 223 closed real interval $\Lambda_r = [-\pi/2, \pi/2]$ connecting the two complex semi-infinite branches
 224 $\Lambda_i^- = -\pi/2 + i(0, \infty)$ and $\Lambda_i^+ = \pi/2 - i(0, \infty)$, so that $\Lambda = \Lambda_i^- \cup \Lambda_r \cup \Lambda_i^+$. A value of
 225 $\phi \in \Lambda_r$ corresponds to a travelling plane wave component at angle ϕ with respect to
 226 the x -axis, while $\phi \in \Lambda_i^\pm$ corresponds to an evanescent wave decaying exponentially
 227 with x . These evanescent wave components arise from wave sources in the adjacent
 228 rows, which will be discussed later, and must therefore be considered if the rows are
 229 not widely spaced [see 34].

230 We seek to characterise the outgoing wave field from row s in the form

$$p_-^s = \int_{\Lambda} B_s^-(\chi) e^{i k(-(x-\xi_{s-1}) \cos \phi + y \sin \phi)} d\phi, \quad x \leq \xi_{s-1} \quad (29)$$

231 for the leftward components and

$$p_+^s = \int_{\Lambda} B_s^+(\chi) e^{ik((x-\xi_s)\cos\phi+y\sin\phi)} d\phi, \quad x \geq \xi_s \quad (30)$$

232 for the rightward components, where the amplitude functions $B_s^\pm(\chi)$ are the unknowns
233 to be determined.

234 The multipole expansion Eq. (24) for the incident field p_{inc}^s is obtained from the
235 Jacobi expansion [13, Eq. (2.17)]. The coefficients f_n^j in expansion (24) are then given
236 by

$$f_n^j = \int_{\Lambda} (i^n e^{-in\phi} A_s^+(\phi) + (-i)^n e^{in\phi} A_s^-(\phi)) e^{ik((d/2)\cos\phi+y_j\sin\phi)} d\phi. \quad (31)$$

237

In response to the incident wave forcing p_{inc}^s , a scattered field is produced by the
array of scatterers in row s . It is given by

$$\begin{aligned} p_{\text{scat}}^s(x, y) &\approx \sum_{j=1}^{J_c} \sum_{n=-N}^N c_n^j H_n(kr_j) e^{in\theta_j} \\ &= \sum_{j=1}^{J_c} \sum_{n=-N}^N c_n^j \frac{(\mp i)}{\pi} \int_{\Lambda} e^{\pm in\chi} e^{ik(\pm(x-x_s)\cos\chi+(y-y_j)\sin\chi)} d\chi, \quad \pm(x-x_s) \geq 0. \end{aligned} \quad (32)$$

238 In the last step, we used a plane wave expansion of the outgoing polar harmonics derived
239 in [34]. This expansion justifies the range integration Λ used in Eq. (28).

240 Combining Eqs. (31), (27) and (32), we obtain after some algebra the following
241 integral mappings relating the amplitude functions of the outgoing wave fields to those

242 of the incoming wave fields

$$B_s^-(\chi) = \int_{\Lambda} (\mathcal{R}^-(\chi : \phi)A_s^+(\phi) + \mathcal{T}^-(\chi : \phi)A_s^-(\phi)) d\phi \quad (33)$$

$$B_s^+(\chi) = \int_{\Lambda} (\mathcal{T}^+(\chi : \phi)A_s^+(\phi) + \mathcal{R}^+(\chi : \phi)A_s^-(\phi)) d\phi \quad (34)$$

243 where $\mathcal{R}^\pm(\chi : \phi)$ and $\mathcal{T}^\pm(\chi : \phi)$ are the reflection and transmission kernels. Semi-
 244 analytical expressions for these kernels can be obtained and the reader is referred to
 245 [34] for the full derivation.

246 For numerical purposes, Eqs. (33) and (34) are discretised by (i) truncating the
 247 complex branches Λ_i^\pm to $\pm\pi/2 \mp 2i$ (a value shown to generate errors close to machine
 248 precision by Montiel et al. [41]), (ii) sampling the angular parameters ϕ and χ over the
 249 truncated version of Γ and (iii) using a numerical quadrature (e.g. the trapezoidal rule)
 250 for the integration. This yields the matrix mapping

$$\begin{pmatrix} \mathbf{B}_s^- \\ \mathbf{B}_s^+ \end{pmatrix} = \begin{pmatrix} \mathbf{R}^- & \mathbf{T}^- \\ \mathbf{T}^+ & \mathbf{R}^+ \end{pmatrix} \begin{pmatrix} \mathbf{A}_s^+ \\ \mathbf{A}_s^- \end{pmatrix} = \mathbf{S} \begin{pmatrix} \mathbf{A}_s^+ \\ \mathbf{A}_s^- \end{pmatrix}, \quad (35)$$

251 where \mathbf{A}_s^\pm and \mathbf{B}_s^\pm are column vectors containing the sampled values of the correspond-
 252 ing amplitude functions. Similarly the matrices \mathbf{R}^\pm and \mathbf{T}^\pm contain the sampled values
 253 of the reflection and transmission kernels and also incorporate the quadrature weights.

254 Wave interaction between rows is enforced by writing $\mathbf{B}_s^- = \mathbf{A}_{s-1}^-$ and $\mathbf{B}_s^+ = \mathbf{A}_{s+1}^+$,
 255 so that outgoing waves from row s are incident wave forcings on the adjacent rows $s - 1$
 256 and $s + 1$. Therefore, the only amplitude vectors to consider are \mathbf{A}_s^\pm for $s = 0, \dots, S$,
 257 with \mathbf{A}_0^+ and \mathbf{A}_S^- prescribed and the other vectors unknown of the problem. The

258 ambient pressure field given in Eq. (3) is used to set \mathbf{A}_0^+ , while \mathbf{A}_S^- is assumed to be
 259 zero (there are no waves incident from the right). A version of the so-called S -matrix
 260 method is used to solve for the unknown amplitude vectors iteratively [see 34].

The transmitted pressure field through the array is obtained directly from Eq. (28)

$$\begin{aligned}
 p_T(x, y) &= \int_{\Lambda} A_S^+(\chi) e^{ik((x-\xi_s)\cos\chi + y\sin\chi)} d\chi \\
 &\approx \int_{\Lambda_r} A_S^+(\chi) e^{-ik\xi_s\cos\chi} e^{ik(x\cos\chi + y\sin\chi)} d\chi.
 \end{aligned}
 \tag{36}$$

261 This latter approximation is valid in the far field, that is $x \gg \xi_s$ where the complex
 262 branches do not contribute. In addition, it is identical to the expression of the pressure
 263 field given in Eq. (4) with transmitted amplitude

$$A_T(\chi) = A_S^+(\chi) e^{-ik\xi_s\cos\chi}. \tag{37}$$

264 To compute the transmitted pressure at any point (x, y) , we integrate Eq. (36) numer-
 265 ically.

266 4. Numerical method

A 2D finite element model of a 5×51 square lattice sonic crystal comprising sound-
 hard cylinders or C-shaped resonators was developed using the commercial software
 COMSOL Multiphysics (v5.1). In the finite element method a weak formulation of
 the Helmholtz equation is solved. By introducing the weak formulation with weighting

function $\Psi(\mathbf{x})$, the Helmholtz equation is transformed as follows [35]

$$\int_{\Omega} \nabla \Psi(\mathbf{x}) \cdot \nabla p(\mathbf{x}) - k^2 \Psi(\mathbf{x}) p(\mathbf{x}) \, d\Omega(\mathbf{x}) - i\rho_f c_f \int_{\Gamma} \Psi(\mathbf{x}) Y(\mathbf{x}) p(\mathbf{x}) \, d\Gamma(\mathbf{x}) = i\rho_f c_f \int_{\Gamma} \Psi(\mathbf{x}) v_s(\mathbf{x}) p(\mathbf{x}) \, d\Gamma(\mathbf{x}) \quad (38)$$

267

268 where ρ_f is the fluid density, c_f is the speed of sound in the fluid medium and Γ is
 269 the boundary surface of the body. Ω represents the acoustic domain. v_s is the particle
 270 velocity of the structure and $Y(\mathbf{x})$ is the boundary admittance. The acoustic pressure
 271 on each element can be discretised as follows

$$p(\mathbf{y}) = \sum_{i=1}^M \Phi_i(\mathbf{x}) p_i \quad (39)$$

272 where $\Phi_i(\mathbf{y})$ are interpolation functions, M is the number of nodal points in each
 273 element and p_i represents the acoustic pressure at nodal points. Substituting equation
 274 (39) into equation (38) yields

$$[\mathbf{K}] - k^2[\mathbf{M}] \{\mathbf{p}\} = \{\mathbf{f}\} \quad (40)$$

275 where \mathbf{K} and \mathbf{M} are the stiffness and mass matrices of the acoustic domain, respectively.
 276 The excitation vector \mathbf{f} represents the source and the pressure vector \mathbf{p} represents the
 277 sound pressure values at the nodal locations in the acoustic domain. The entries of the

278 stiffness and mass matrices are given by

$$m_{ij} = \int_{\Omega} \Phi_i(\mathbf{x}) \Phi_j(\mathbf{x}) d\Omega(\mathbf{x}) \quad (41)$$

$$k_{ij} = \int_{\Omega} \nabla \Phi_i(\mathbf{x}) \cdot \nabla \Phi_j(\mathbf{x}) d\Omega(\mathbf{x}) \quad (42)$$

279 The acoustic domain in the finite element model was discretised using triangular
 280 elements. A perfectly matched layer was applied on the boundary of the acoustic domain
 281 to allow the outgoing sound waves to leave the domain with minimal reflections. A fine
 282 mesh was used for all the numerical models to ensure accurate numerical predictions.
 283 The largest element size was less than 1/6 the wavelength at the highest frequency
 284 considered in this work. Figure 2 shows a truncated domain in the y -direction of 5 rows
 285 of solid circular scatterers in a square lattice arrangement under incident plane wave
 286 excitation. The boundary conditions and the shadow zone of the array are also shown.

287 5. Results and discussion

288 For all the results in this section, we consider a sonic crystal composed $S = 5$ rows,
 289 each containing $J_c = 51$ scatterers (justified later). We fix the radius of the scatterers to
 290 $a=0.2$ m and the spacing between adjacent scatterers to $d=0.6$ m. The air background
 291 medium is assumed to have density $\rho_f \approx 1.21$ kg/m³ and speed of sound $c_f \approx 343$ m/s.

292 Sound attenuation by the sonic crystal array is quantified using the sound transmis-
 293 sion loss, which is expressed in decibels as the ratio of the acoustic energy in the shadow
 294 zone of the array to the acoustic energy incident on the array, that is, $10\log_{10}(p_T^2/p_{\text{inc}}^2)$.

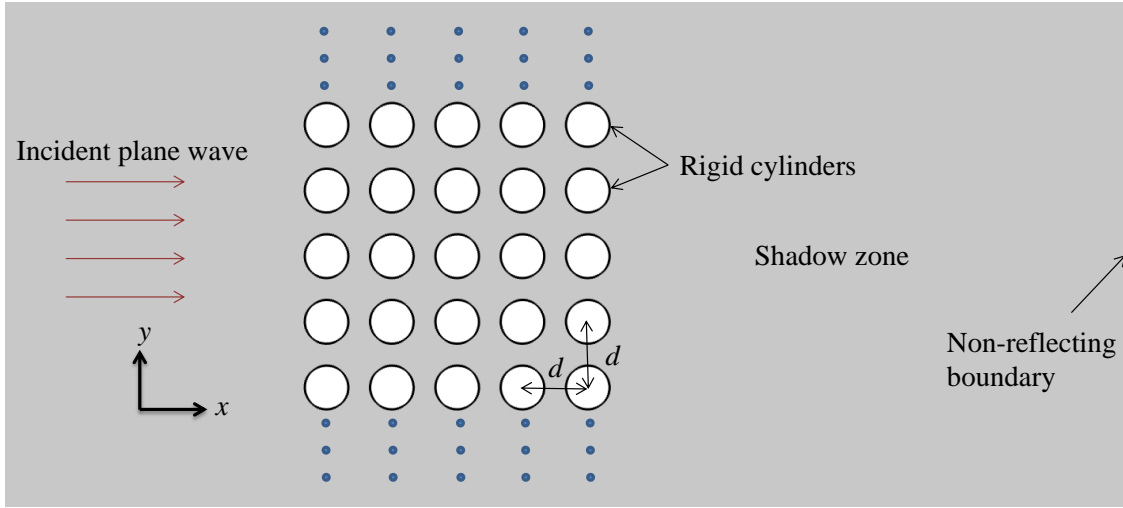


Figure 2: 2D domain used in the finite element model of a 5×51 sonic crystal lattice using cylindrical scatterers under incident plane wave excitation.

295 The incident plane wave is always normal to the barrier. The point receiver location
 296 is at the centre of the array in the y -direction and 3 m from the centre of the last row
 297 of cylinders in the shadow zone. The transmitted pressure at this point is computed
 298 using both Eqs. (36) and (39) corresponding to the analytical solution described in §3
 299 and the numerical solution described in §4, respectively.

300 Figure 3 presents the transmission loss as a function of frequency for a sonic crystal of
 301 sound-hard scatterers. As a benchmark, the transmission loss obtained numerically for
 302 5 infinite rows of scatterers using periodic boundary conditions in the y -direction is also
 303 shown. At frequencies around peak transmission loss, the scattered sound waves within
 304 the sonic crystal array destructively interfere, resulting in a maximum of around 40 dB
 305 attenuation for 5 rows of scatterers. This feature is associated with an approximation of
 306 the first Bragg band gap of the corresponding doubly infinite array, as the highest sound
 307 transmission loss for an infinite number of scatterers in the y -direction occurs around

308 270 Hz which approximately corresponds to the centre frequency predicted by Bragg's
 309 law, which is given by $f_B = c_f/2d$ [4]. The effect of having a finite number of scatterers
 310 in the y -direction is observed to only affect the maximum transmission loss occurring
 311 within the Bragg band gap. For frequencies outside of the stop band gap, the sound
 312 waves are mostly unaffected and pass freely through the sonic crystal array. Very good
 313 agreement in the results from the analytical and numerical models can be observed,
 314 with small variations only occurring at frequencies around maximum transmission loss.
 315 A convergence analysis (not shown here) showed that by fixing $J_c = 51$, the optimal
 316 number of rows for approximating the Bragg band gap is $S = 5$. This provides a
 317 justification for the size of the sonic crystal considered here.

318 Figure 4 shows the transmission loss as a function of frequency for a sonic crystal of
 319 C-shaped resonators. For comparison, the transmission loss obtained numerically for 5
 320 infinite rows of C-shaped and sound-hard scatterers is also indicated. We observe an
 321 extra peak in transmission loss at low frequencies for the array of resonators, in addition
 322 to the Bragg band gap. The peak frequency of this sub-Bragg band gap is related to
 323 the resonant frequency of the Helmholtz resonator, which is given as follows [42]

$$f_{\text{HR}} = \frac{c_f}{2\pi} \sqrt{\frac{e}{l_{eq}\pi R^2}} \quad (43)$$

324 where e is the opening length of the resonator, R is the inner radius of the shell,
 325 $l_{eq} = t + 0.85e$ is the equivalent length and t is the shell thickness. For small shell
 326 thickness, $e = 2R\sin\alpha$. A shell thickness of 0.01 m was used in the FEM model.
 327 Although not shown here, increasing or reducing the shell thickness from the chosen
 328 value was not found to affect the numerical results.

329 For an infinite array of C-shaped cylindrical shell scatterers, a very significant peak
330 in transmission loss occurs at the Helmholtz resonator frequency. The peak is reduced
331 for a finite number of scatterers attributed to the interference of circular waves in the
332 shadow zone generated by the scatterers near the edges of the array. Using the C-shaped
333 scatterers, the lower frequency of the band gap due to Bragg scattering is shifted to a
334 higher frequency compared with the band gap obtained using solid cylinder scatterers.
335 Furthermore, the overall transmission loss associated with Bragg scattering using the
336 C-shaped scatterers is reduced.

337 Figures 5–8 present contour fields obtained numerically of the sound pressure level
338 at discrete frequencies for the cylindrical and C-shaped scatterers. The incident plane
339 wave is clearly observed in all figures. Figure 5 shows that for a finite array of cylinders
340 at 270 Hz, the greatest reduction in the sound pressure level occurs in a region around
341 the receiver location in the barrier shadow zone. In contrast, at 400 Hz in Figure 6,
342 with the exception of diffraction around the edges of the finite array, the sound waves
343 are mostly unaffected by the periodic arrangement of cylinders and pass freely through
344 the sonic crystal. Figures 7 and 8 present contour fields of the sound pressure level for
345 the C-shaped scatterers at the local resonant frequency of the scatterers correspond-
346 ing to 135 Hz (Figure 7) as well as at a frequency of 285 Hz corresponding to peak
347 transmission loss due to the periodicity of the scatterer array (Figure 8). Figure 7
348 shows that the reduction in pressure in the barrier shadow zone is clearly attributed
349 to sound absorption by the scatterers acting as Helmholtz resonators. Figure 8 shows
350 that the mechanism for sound reduction in the barrier shadow zone is attributed to the
351 destructive interference of sound waves within the crystal structure due to the periodic
352 arrangement of the scatterers.

353 Figure 9 compares the analytical and numerical results for different opening angles.
354 A similar trend in the results obtained analytically and numerically can be observed.
355 Figure 10 presents the effect of increasing the size of the opening angle of the C-shaped
356 cylindrical shell scatterers on the transmission loss obtained analytically. With an
357 increase in the size of the opening angle, there is a shift in the location of peak trans-
358 mission loss associated with the Helmholtz resonator frequency to a higher frequency, as
359 confirmed by Eq. (43). The lower frequency of the Bragg band gap is also significantly
360 affected by the size of the opening of the C-shaped cylindrical shells.

361 Figure 11 presents the analytical and numerical results for different location of
362 opening around the circumference of the C-shaped cylindrical shells with respect to the
363 incident plane wave. The opening angle of the scatterers is constant at 30° . To compare
364 the effect of rotating the location of the opening, the analytical results are presented
365 in Figure 12. A rotation of 0° corresponds to the opening of the C-shaped scatterers
366 directly facing towards the incident plane wave as shown in Figure 1. A rotation of 180°
367 corresponds to the opening of the C-shaped scatterers facing towards the shadow zone of
368 the array. Grazing incidence occurs for a rotation of 90° . An increase in the bandwidth
369 due to Bragg scattering occurs for grazing incidence. Good agreement between the
370 analytical and numerical results for all orientation angles can be observed.

371 **6. Summary**

372 Analytical and numerical models of a finite sonic crystal array using sound-hard
373 cylinders and C-shaped resonators have been presented. For a sonic crystal array com-
374 prising sound-hard cylinders, a broad band gap was generated due to the phenomenon
375 of Bragg resonance destructively interfering waves travelling through a periodic array.

376 With the use of the resonators, a narrow band gap in transmission loss in addition to
377 the stop band gap due to Bragg scattering, was shown to occur at low frequencies and
378 is related to the frequency of a Helmholtz resonator. Our study suggests that relatively
379 small finite arrays can reproduce accurately the theoretical band structure of infinite
380 crystals, which is important for practical applications.

381 **References**

- 382 [1] E. N. Economou, M. Sigalas, Stop bands for elastic waves in periodic composite
383 materials, *J Acoust Soc Am* 95 (1994) 1734–1740.
- 384 [2] R. Martinez-Sala, J. Sancho, J. V. Sanchez, V. Gomez, J. Llinares, F. Meseguer,
385 Sound attenuation by sculpture, *Nature* 378 (1995) 241–241.
- 386 [3] J. V. Sanchez-Perez, C. Rubio, R. Martinez-Sala, R. Sanchez-Grandia, V. Gomez,
387 Acoustic barriers based on periodic arrays of scatterers, *Appl Phys Lett* 81 (2002)
388 5240–5242.
- 389 [4] F. Koussa, J. Defrance, P. Jean, P. Blanc-Benon, Acoustical efficiency of a sonic
390 crystal assisted noise barrier, *Acta Acust United Ac* 99 (2013) 399–409.
- 391 [5] M. A. Peter, M. H. Meylan, Water-wave scattering by a semi-infinite periodic
392 array of arbitrary bodies, *J Fluid Mech* 575 (2007) 473–494.
- 393 [6] L. G. Bennetts, Wave attenuation through multiple rows of scatterers with differing
394 periodicities, *Siam J Appl Math* 71 (2011) 540–558.
- 395 [7] L. Bennetts, V. Squire, Wave scattering by multiple rows of circular ice floes, *J*
396 *Fluid Mech* 639 (2009) 213–238.

- 397 [8] V. Leroy, A. Bretagne, M. Fink, H. Willaime, P. Tabeling, A. Tourin, Design and
398 characterization of bubble phononic crystals, *Appl Phys Lett* 95 (2009) 171904.
- 399 [9] D. C. Calvo, A. L. Thangawng, C. N. Layman Jr, R. Casalini, S. F. Othman,
400 Underwater sound transmission through arrays of disk cavities in a soft elastic
401 medium, *J Acoust Soc Am* 138 (2015) 2537–2547.
- 402 [10] A. Asatryan, P. Robinson, L. Botten, R. McPhedran, N. Nicorovici, C. M.
403 de Sterke, Effects of disorder on wave propagation in two-dimensional photonic
404 crystals, *Phys Rev E* 60 (1999) 6118–6127.
- 405 [11] C. Linton, I. Thompson, Resonant effects in scattering by periodic arrays, *Wave*
406 *Motion* 44 (2007) 165–175.
- 407 [12] C. Linton, D. Evans, The interaction of waves with arrays of vertical circular
408 cylinders, *J Fluid Mech* 215 (1990) 549–569.
- 409 [13] P. A. Martin, Multiple scattering: interaction of time-harmonic waves with N ob-
410 stacles, volume 10, Issue 107 of *Encyclopedia of Mathematics and Its Applications*,
411 Cambridge University Press, 2006.
- 412 [14] Y.-Y. Chen, Z. Ye, Theoretical analysis of acoustic stop bands in two-dimensional
413 periodic scattering arrays, *Phys Rev E* 64 (2001) 036616.
- 414 [15] B. van der Aa, J. Forssén, Scattering by an array of perforated cylinders with a
415 porous core, *J Acoust Soc Am* 136 (2014) 2370–2380.
- 416 [16] M. S. Kushwaha, P. Halevi, L. Dobrzynski, B. Djafari-Rouhani, Acoustic band
417 structure of periodic elastic composites, *Phys Rev Lett* 71 (1993) 2022.

- 418 [17] T. Miyashita, Sonic crystals and sonic wave-guides, *Meas Sci Technol* 16 (2005)
419 R47.
- 420 [18] A. Gupta, A review on sonic crystal, its applications and numerical analysis tech-
421 niques, *Acoust Phys* 60 (2014) 223–234.
- 422 [19] A. Gupta, K.-M. Lim, C. H. Chew, Design of radial sonic crystal for sound atten-
423 uation from divergent sound source, *Wave Motion* 55 (2015) 1–9.
- 424 [20] P. Jean, J. Defrance, Sound propagation in rows of cylinders of infinite extent:
425 Application to sonic crystals and thickets along roads, *Acta Acust United Ac* 101
426 (2015) 474–483.
- 427 [21] J. O. Vasseur, P. A. Deymier, A. Khelif, P. Lambin, B. Djafari-Rouhani, A. Akjouj,
428 L. Dobrzynski, N. Fettouhi, J. Zemmouri, Phononic crystal with low filling fraction
429 and absolute acoustic band gap in the audible frequency range: A theoretical and
430 experimental study, *Phys Rev E* 65 (2002) 056608.
- 431 [22] B. van der Aa, J. Forssén, The 2.5D MST for sound propagation through an array
432 of acoustically rigid cylinders perpendicular to an impedance surface, *J Phys D:
433 Appl Phys* 48 (2015) 295501.
- 434 [23] Y.-Y. Chen, Z. Ye, Acoustic attenuation by two-dimensional arrays of rigid cylin-
435 ders, *Phys Rev Lett* 87 (2001) 184301.
- 436 [24] V. Romero-García, J. V. Sánchez-Pérez, L. M. Garcia-Raffi, Analytical model to
437 predict the effect of a finite impedance surface on the propagation properties of
438 2D sonic crystals, *J Phys D: Appl Phys* 44 (2011) 265501.

- 439 [25] G. Ke, Z. C. Zheng, Sound propagation around arrays of rigid and porous cylinders
440 in free space and near a ground boundary, *J Sound Vib* 370 (2016) 43–53.
- 441 [26] Z. Liu, X. Zhang, Y. Mao, Y. Y. Zhu, Z. Yang, C. T. Chan, P. Sheng, Locally
442 resonant sonic materials, *Science* 289 (2000) 1734–1736.
- 443 [27] L.-Y. Wu, L.-W. Chen, Wave propagation in a 2D sonic crystal with a Helmholtz
444 resonant defect, *J Phys D: Appl Phys* 43 (2010) 055401.
- 445 [28] X. Hu, C. T. Chan, J. Zi, Two-dimensional sonic crystals with Helmholtz res-
446 onators, *Phys Rev E* 71 (2005) 055601.
- 447 [29] J.-B. Li, Y.-S. Wang, C. Zhang, Tuning of acoustic bandgaps in phononic crystals
448 with Helmholtz resonators, *J Vib Acoust* 135 (2013) 031015.
- 449 [30] L. Chalmers, D. Elford, F. Kusmartsev, G. Swallowe, Acoustic band gap for-
450 mation in two-dimensional locally resonant sonic crystals comprised of Helmholtz
451 resonators, *Int J Mod Phys B* 23 (2009) 4234–4243.
- 452 [31] A. Krynkin, O. Umnova, S. Taherzadeh, K. Attenborough, Analytical approxima-
453 tions for low frequency band gaps in periodic arrays of elastic shells, *J Acoust Soc*
454 *Am* 133 (2013) 781–791.
- 455 [32] D. P. Elford, L. Chalmers, F. V. Kusmartsev, G. M. Swallowe, Matryoshka locally
456 resonant sonic crystal, *J Acoust Soc Am* 130 (2011) 2746–2755.
- 457 [33] V. Romero-García, A. Krynkin, L. M. Garcia-Raffi, O. Umnova, J. V. Sánchez-
458 Pérez, Multi-resonant scatterers in sonic crystals: Locally multi-resonant acoustic
459 metamaterial, *J Sound Vib* 332 (2013) 184–198.

- 460 [34] F. Montiel, V. A. Squire, L. G. Bennetts, Evolution of directional wave spectra
461 through finite regular and randomly perturbed arrays of scatterers, *Siam J Appl*
462 *Math* 75 (2015) 630–651.
- 463 [35] S. Marburg, B. Nolte, A unified approach to finite and boundary element dis-
464 cretization in linear time-harmonic acoustics, in *Computational Acoustics of Noise*
465 *Propagation in Fluids - Finite and Boundary Element Methods*, Chap. 0, Springer-
466 Verlag, Berlin, 2008.
- 467 [36] A. Norris, G. Wickham, Elastic Helmholtz resonators, *J Acoust Soc Am* 93 (1993)
468 617–630.
- 469 [37] C. M. Linton, P. McIver, *Handbook of mathematical techniques for wave/structure*
470 *interactions*, CRC Press, 2001.
- 471 [38] M. Abramowitz, I. A. Stegun, *Handbook of Mathematical Functions: With For-*
472 *mulas, Graphs, and Mathematical Tables*, Dover, 1970.
- 473 [39] R. C. McPhedran, L. C. Botten, A. A. Asatryan, N. A. Nicorovici, P. A. Robinson,
474 C. M. De Sterke, Calculation of electromagnetic properties of regular and random
475 arrays of metallic and dielectric cylinders, *Phys Rev E* 60 (1999) 7614–7617.
- 476 [40] S. B. Platts, N. V. Movchan, R. C. McPhedran, A. B. Movchan, Twodimensional
477 phononic crystals and scattering of elastic waves by an array of voids, *Proceedings*
478 *of the Royal Society A* (2002).
- 479 [41] F. Montiel, V. A. Squire, L. G. Bennetts, Attenuation and directional spreading
480 of ocean wave spectra in the marginal ice zone, *J Fluid Mech* 790 (2016) 492–522.

481 [42] M. L. Munjal, Acoustics of ducts and mufflers with application to exhaust and
482 ventilation system design, John Wiley & Sons, 1987.

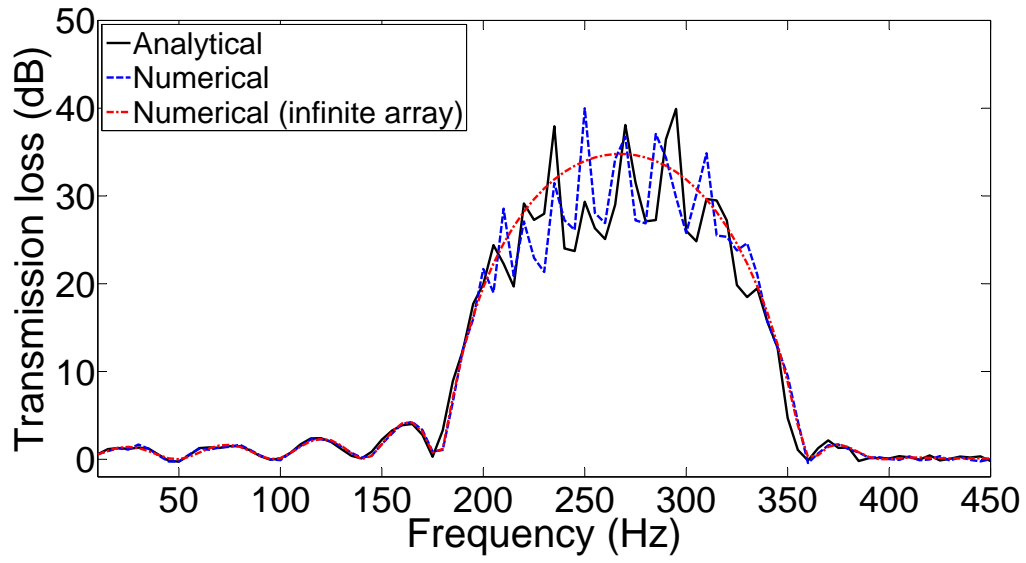


Figure 3: Transmission loss for a finite array of 5×51 cylinders cylinders obtained analytically (black line) and numerically (blue line). Also shown is the transmission loss obtained numerically for 5 rows of cylinders in an infinite array.

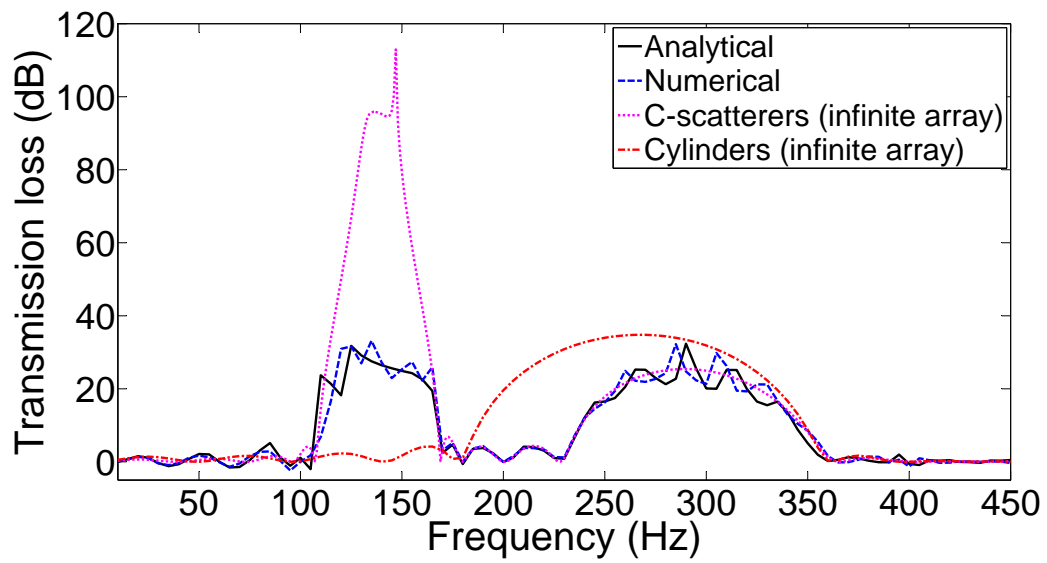


Figure 4: Transmission loss for a finite array of 5×51 C-shaped scatterers obtained analytically (black line) and numerically (blue line). Also shown is the transmission loss obtained numerically for 5 rows of cylinders in an infinite array as well as for 5 rows of C-shaped scatterers in an infinite array. The opening of the C-shaped scatterers is 30° .

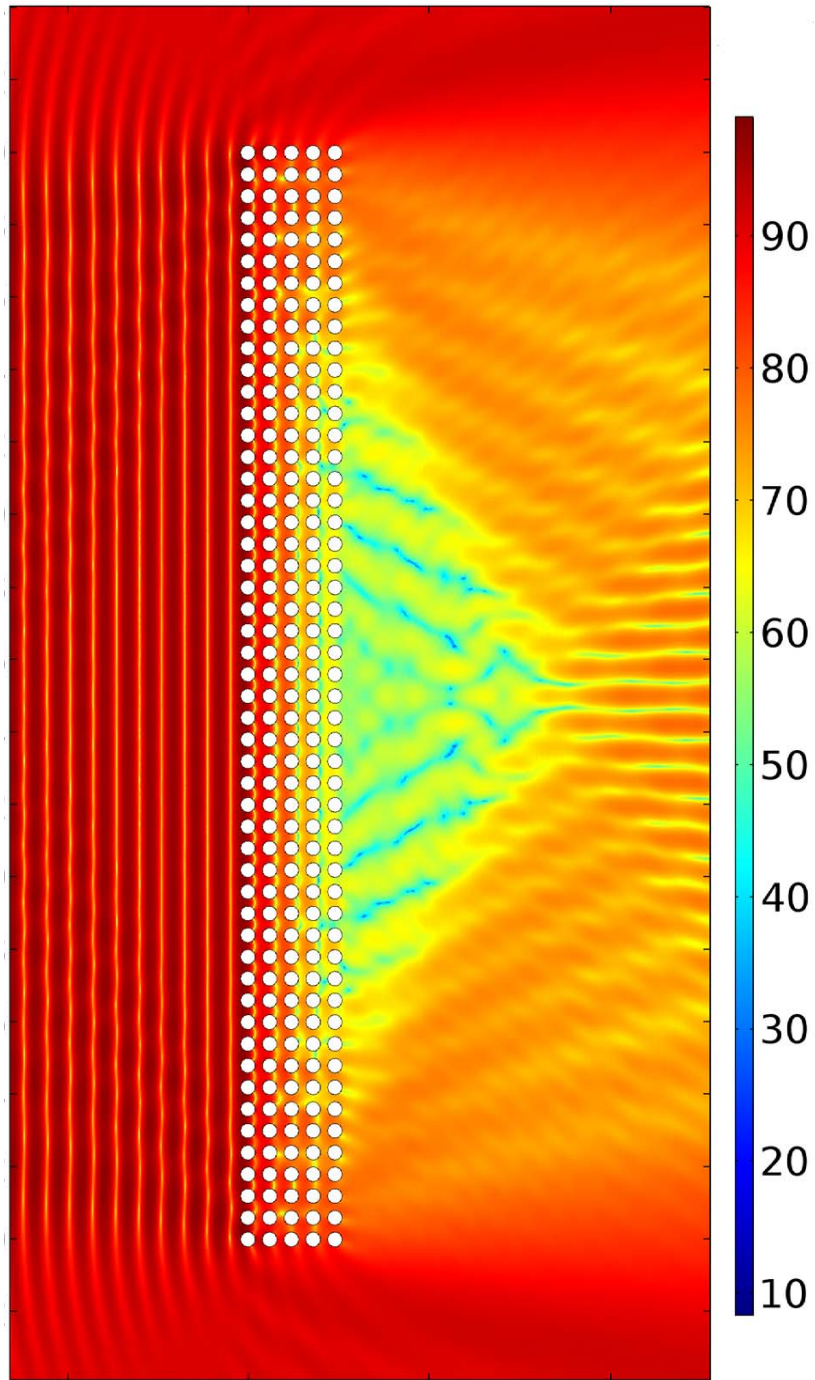


Figure 5: Sound pressure level (dB) obtained numerically for a finite array of 5×51 cylinders at 270 Hz.

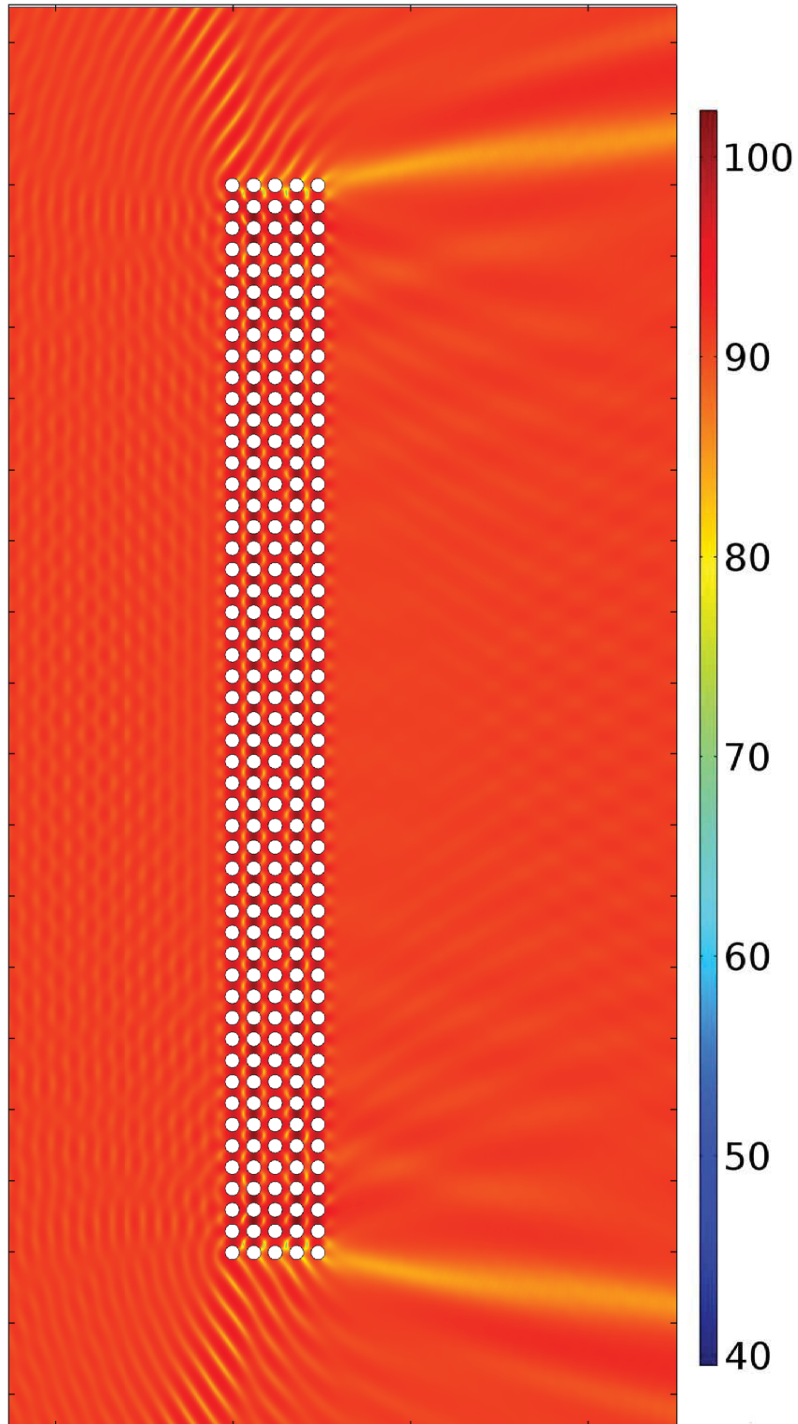


Figure 6: Sound pressure level (dB) obtained numerically for a finite array of 5×51 cylinders at 400 Hz.

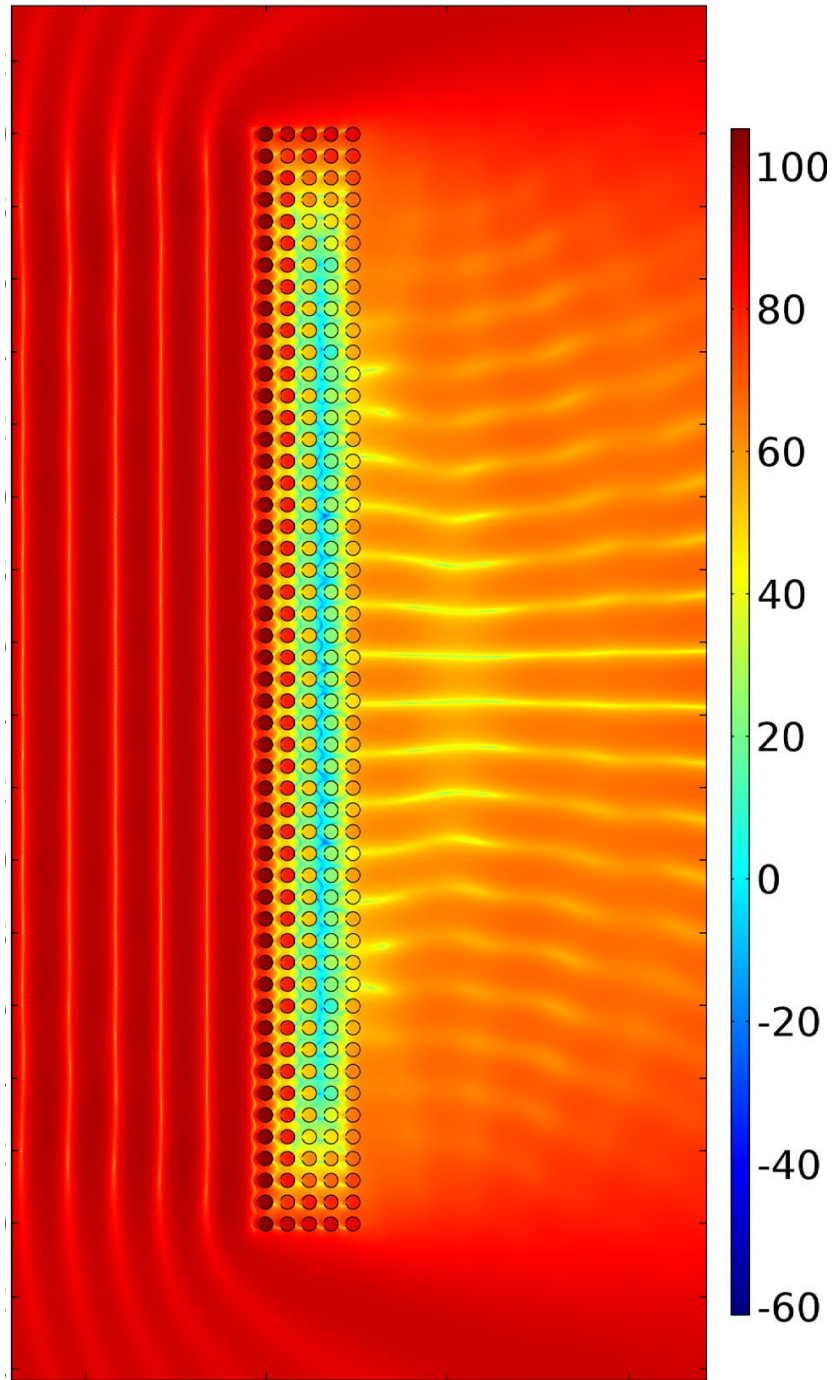


Figure 7: Sound pressure level (dB) obtained numerically for a finite array of 5×51 C-shaped scatterers at 135 Hz.

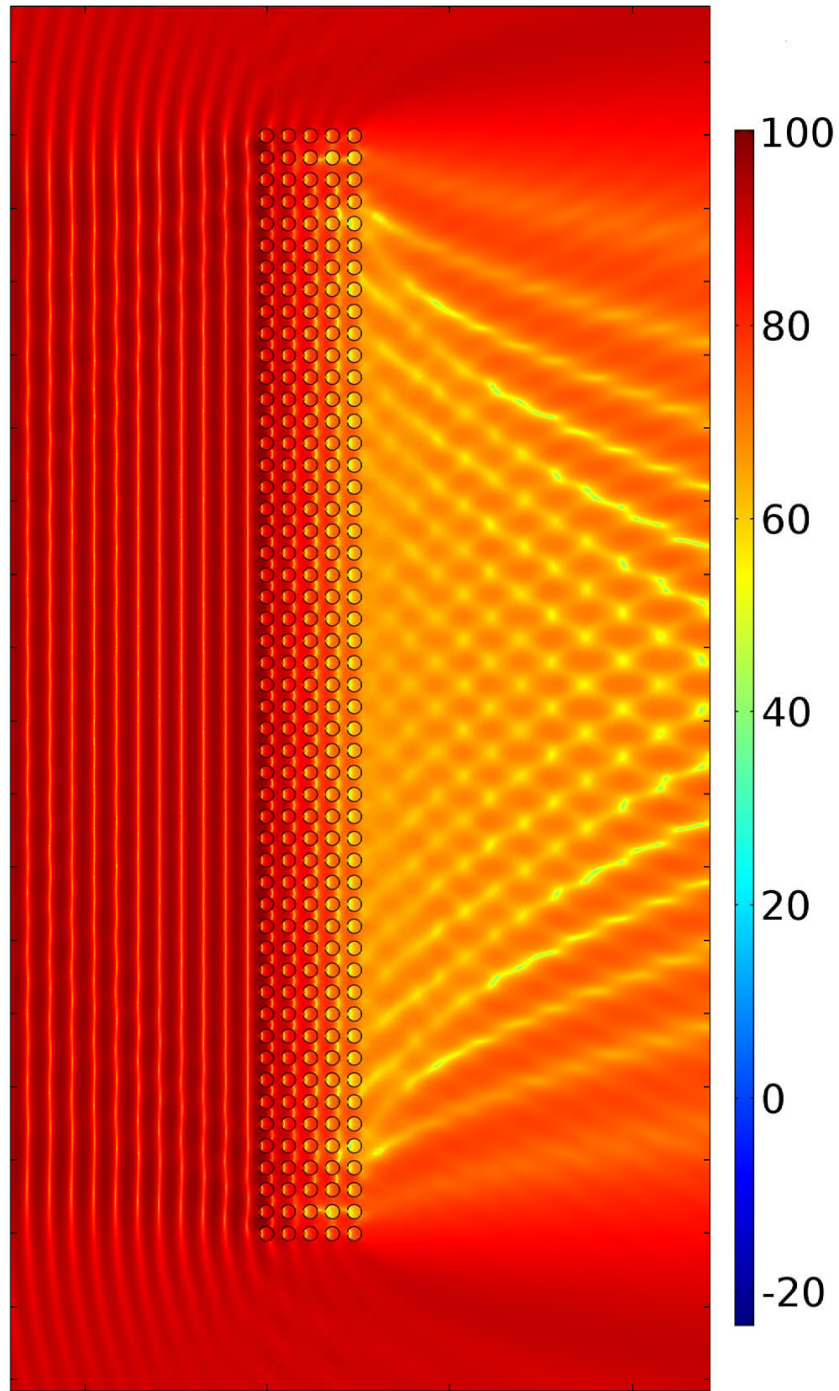
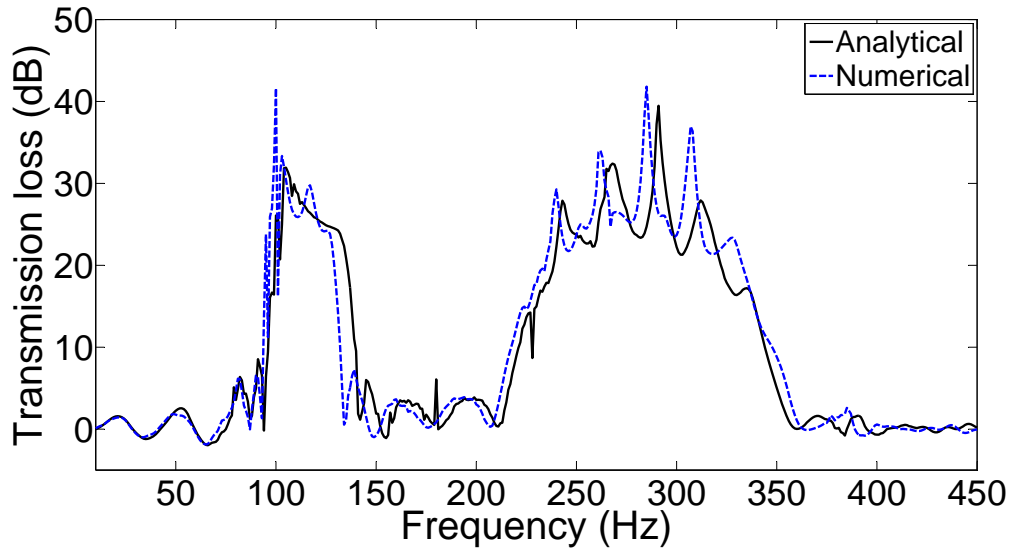
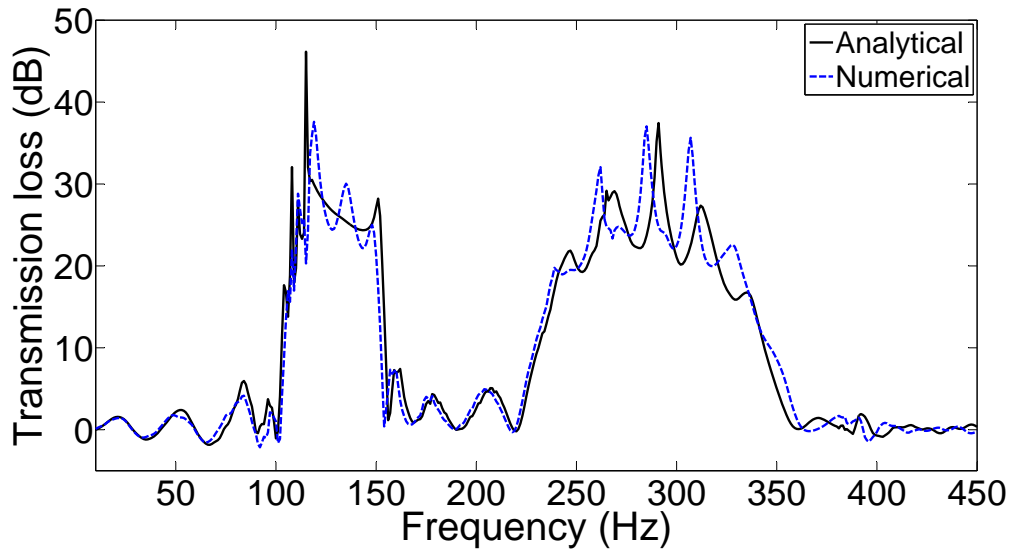


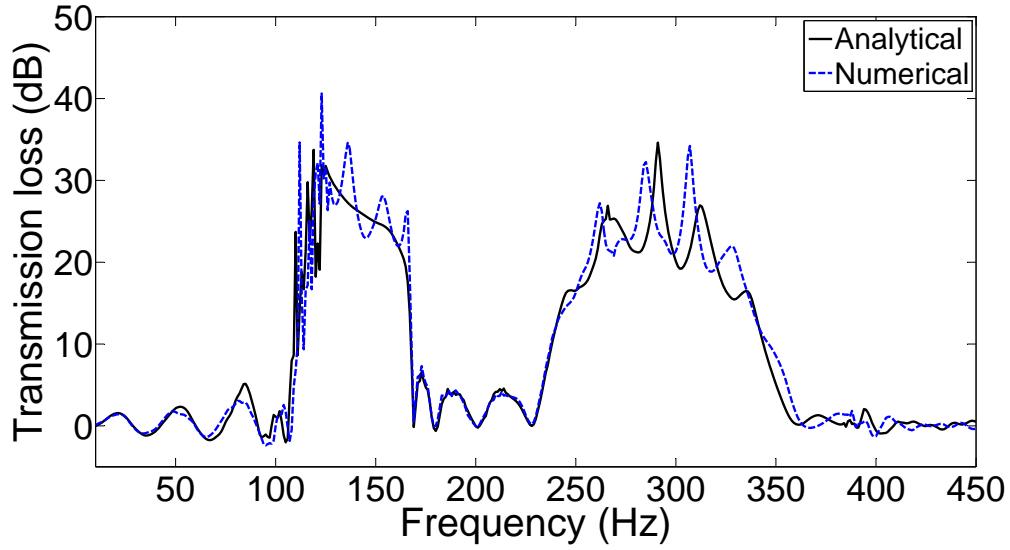
Figure 8: Sound pressure level (dB) obtained numerically for a finite array of 5×51 C-shaped scatterers at 285 Hz.



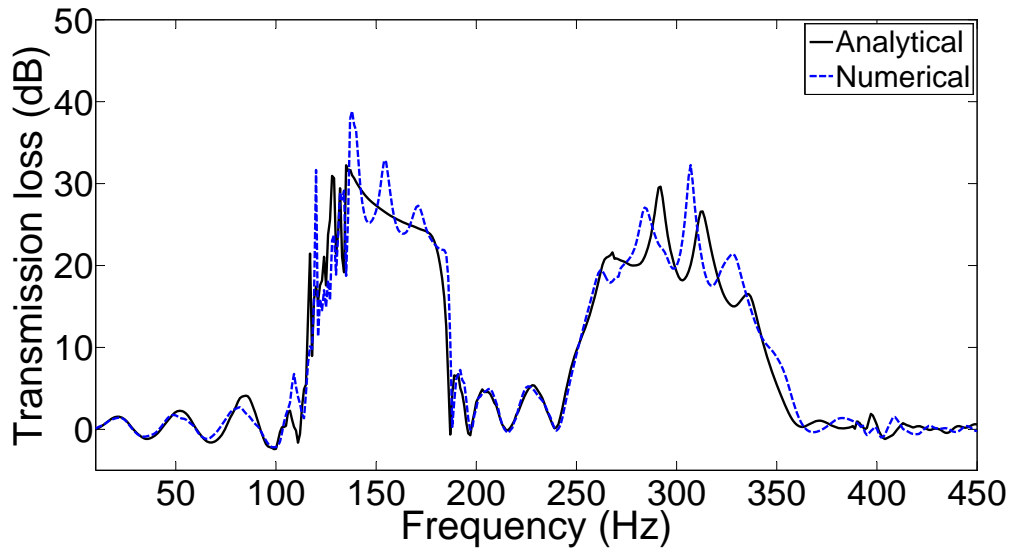
(a)



(b)



(c)



(d)

Figure 9: Transmission loss for a finite array of C-shaped scatterers obtained analytically and numerically for opening angles (a) 10° , (b) 20° , (c) 30° and (d) 45°

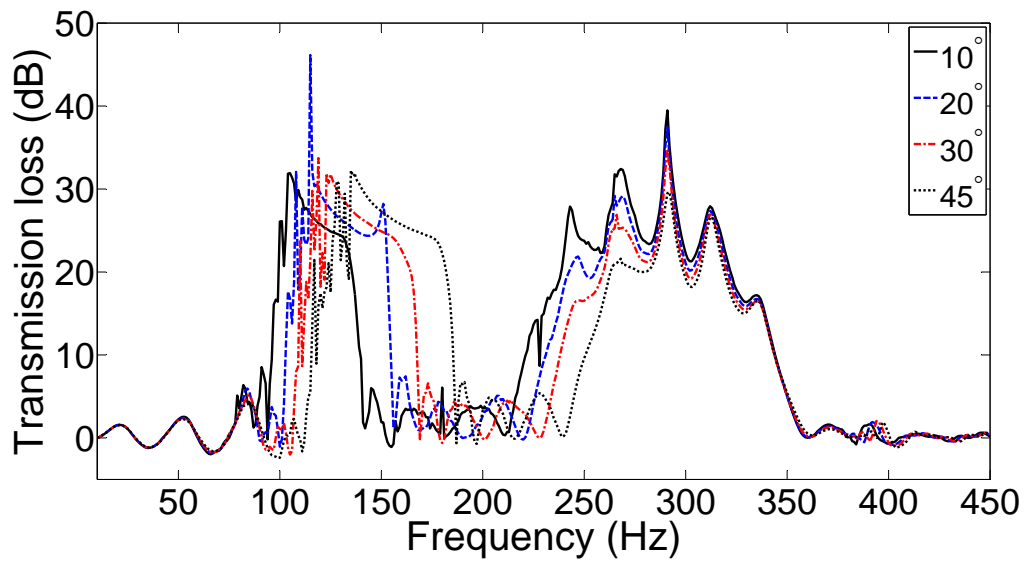
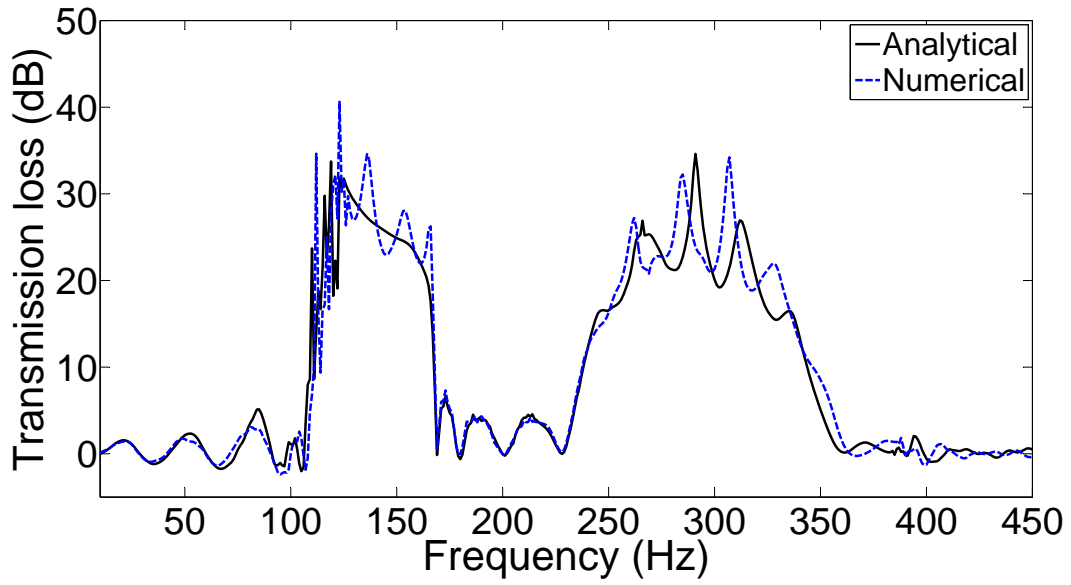
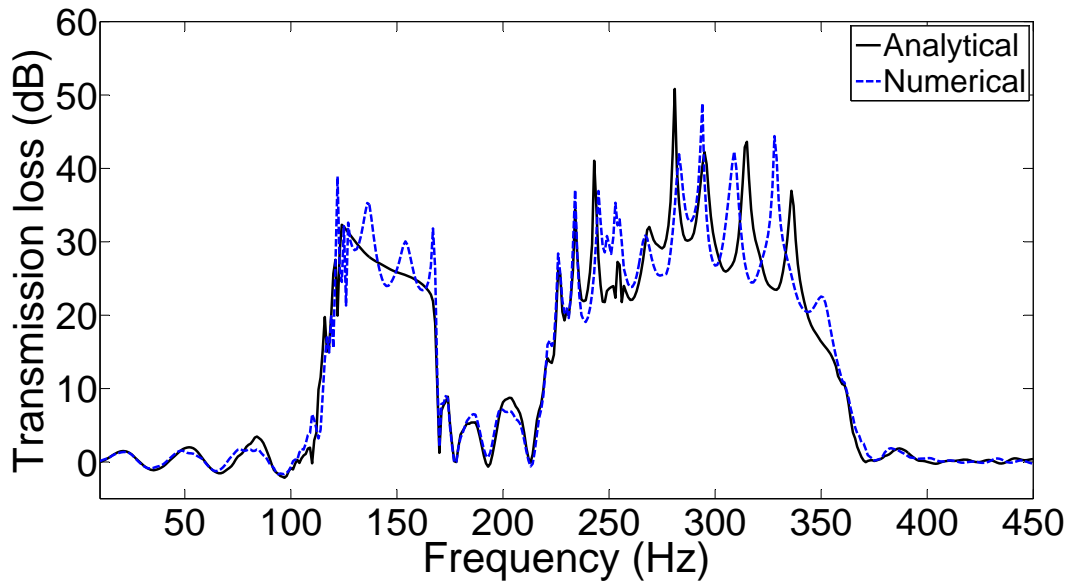


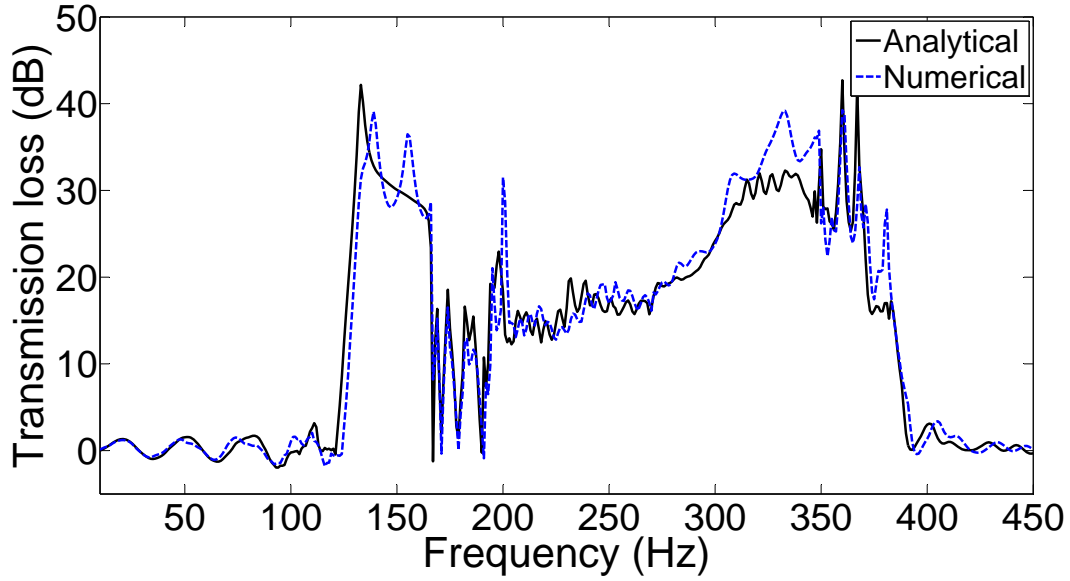
Figure 10: Transmission loss for a finite array of C-shaped scatterers obtained analytically for different opening angles.



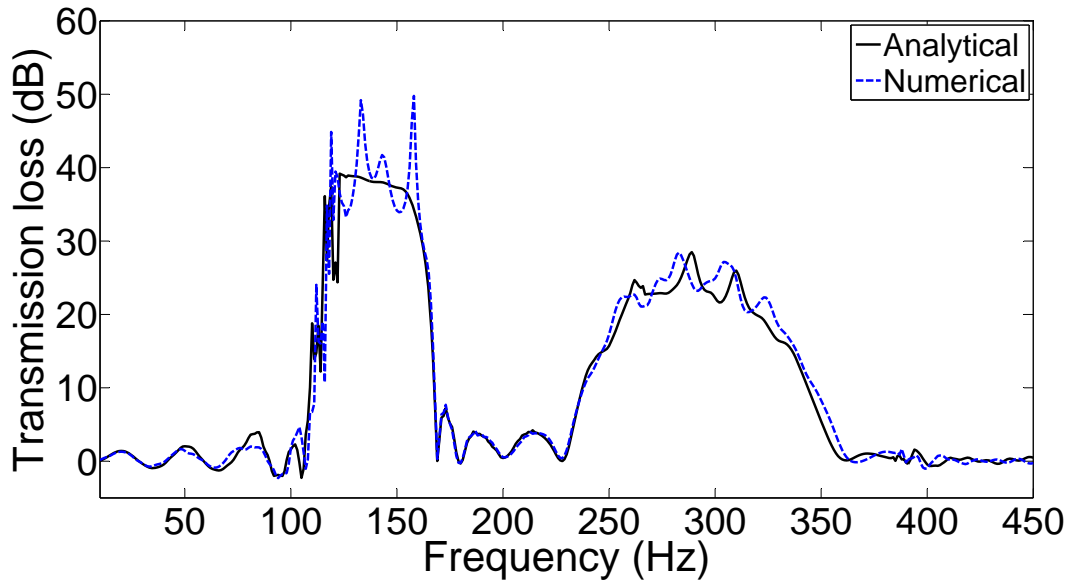
(a)



(b)



(c)



(d)

Figure 11: Transmission loss for a finite array of C-shaped scatterers obtained analytically and numerically for rotation angles (a) 0° , (b) 45° , (c) 90° and (d) 180° , showing the effect of rotating the location of the opening. The opening of the C-shaped scatterers is 30° .

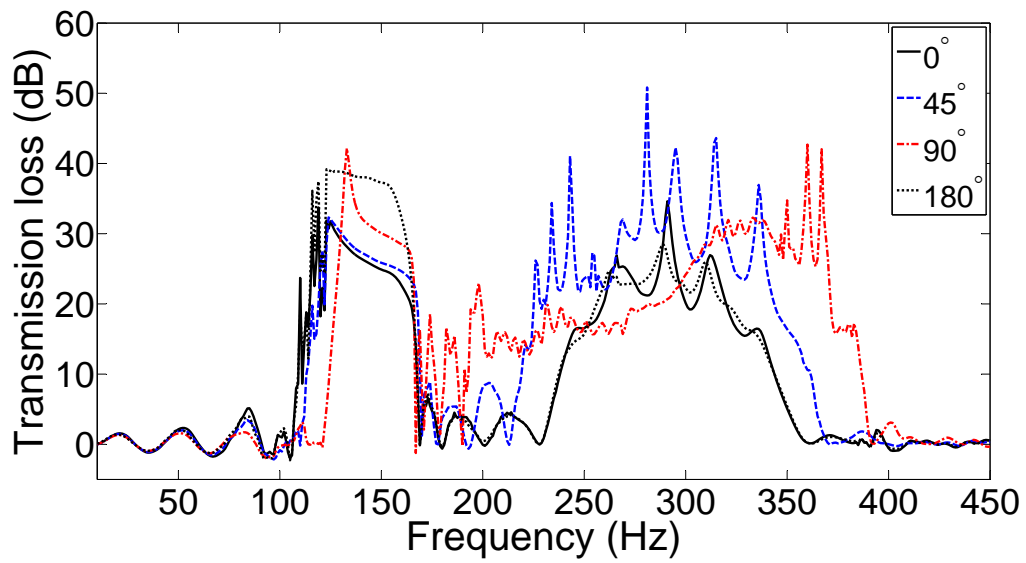


Figure 12: Transmission loss for a finite array of C-shaped scatterers obtained analytically for different rotation angles. The opening of the C-shaped scatterers is 30° .